CrystEngComm

Accepted Manuscript

ROYAL SOCIETY OF CHEMISTRY

www.rsc.org/crystengcomm

(hkl)-specific defects of MgO-CoO alloy by pulsed laser ablation in water

Bang-Ying Chen,[a] Shih-Siang Lin[a], Pouyan Shen[a] and Shuei-Yuan Chen*[b]

[a]*Department of Materials and Optoelectronic Science,*

National Sun Yat-sen University

Kaohsiung, 80424 Taiwan, R.O.C.

[b]*Department of Mechanical and Automation Engineering*

I-Shou University

Kaohsiung, 84001 Taiwan, R.O.C.

* *To whom correspondence should be addressed, e-mail:* steven@isu.edu.tw

Abstract

Metal oxides with (hkl)-specific specific defects of rocksalt-type based structure were fabricated by pulsed laser ablation of powdery MgO-CoO alloy (molar ratio 9:1, 5:5, 1:9 denoted as M9C1, M5C5 and M1C9, respectively against CoO) in water and characterized using transmission electron microscopy. The resultant submicron-sized particles have well-developed {100} surface with {110} edges and abundant dislocations for M9C1, whereas rough surface and paracrystalline distribution of defect clusters (ca. 1.5-2 nm interspacing) along with spinel-type intergrowth for Co-richer compositions. Such paracrystal tended to form arrays following the ~{111} vicinal planes of the rocksalt-type host, i.e. {112} and {113} for M5C5 and {115} for $Co_{1-x}O$ under the influence of mutual dopant and/or the hydrogenation effect. A stable $[110](\bar{1}11)/(\bar{1}12)$ asymmetrical tilt boundary with fair coincidence site lattice also occurred by ~{111}-specific coalescence of the spinel particles for M1C9 specimen. The composition dependent formation of paracrystalline distribution of defect clusters and internal compressive stress (up to ca. 1 GPa) of the rocksalt-type host with characteristic UV-absorbance are addressed.

1. Introduction

The motivation of this research is to fabricate hydrogenated (Mg_xCo_{1-x})O protoxide and Mg-doped $Co_{3-\delta}O_4$ spinel via a dynamic pulsed laser ablation (PLA) route in water regarding the (hkl)-specific defects of the particles, in particular the paracrystalline distribution of defect clusters following specific crystallographic planes and the special grain boundary of the spinel phase, which did not occur by conventional heating/annealing or PLA of metal oxides in air as summarized in our inter-related work,[1] nor known in natural occurrence.

Under equilibrium condition in air, the MgO-$Co_{1-x}O$ binary was known to form a complete solid solution of (Mg_xCo_{1-x})O with rocksalt-type structure at high temperatures which decomposes below 850°C into Mg-doped (<1 at%) $Co_{3-\delta}O_4$ spinel and rocksalt-type protoxide of a wide Co/(Mg+Co) atomic ratio decreasing drastically from 99% to ca. 2% upon cooling from 850°C to 600°C (ref.[2] cf. also Fig. 51 of ref.[3]). However, stoichiometric $MgCo_2O_4$ with an almost ideal inverse spinel structure was also metastabilized by a coprecipitation method in aqueous solution.[4] Analogous to the periclase/brucite (MgO/$Mg(OH)_2$) linkage for the Mg-rich end member, $Co_{1-x}O$ tends to be hydroxylated in humid air as layer double hydroxide (LDH), i.e. $Co(OH)_2$ with plate-like shape which affects significantly the onset coarsening/coalescence kinetics in air.[5] The $Co_{1-x}O$ protoxide also tends to be stabilized as $Co_{3-x}O_4$ spinel below ca. 900°C under ambient air condition.[6]

The bulk sample of $Co_{1-x}O$ with multiple transition metal ions, i.e. Co^{3+} and Co^{2+}, was also known to form rocksalt-type $Co_{1-x}O$ and spinel-type $Co_{3-\delta}O_4$ with paracrystalline distribution of defect clusters when prepared by a sintering-annealing route in air without dopant[7] or doped with quartervalent Zr[8] and divalent Mg[9,10] to tailor the interspacing of the defect clusters. However, such paracrystals hardly form array along a specific crystallographic habit plane of the rocksalt- or spinel-type host. For example, the paracrystalline spinel phase occurred as irregular domains in the C8M2 sample (i.e. $Co_{1-x}O$ and MgO in 8:2 molar ratio) subject to sintering at 1600°C for 5 h in air (cf. Fig. 2 of Ref.[10]).

Regarding the clean/dynamic synthesis of $Co_{1-x}O$, PLA of Co target in an oxygen background gas has been used to condense $Co_{1-x}O$ nanocrystals with cubic shape yet negligible defect clusters and hydroxylation.[11] Such $Co_{1-x}O$ nanocrystals tended to coalesce over cube {100} faces to form nanochain aggregate or in a closer packed manner.[11] Whereas PLA of bulk MgO-$Co_{1-x}O$ alloys in air allowed the formation of dense rocksalt-type nanocondensates with tailored paracrystalline distribution of defect clusters (ca. 1.5-2 nm interspacing), internal compressive stress (up to ca. 2 GPa) and well-developed {100} faces for coalescence as (100) 26.6^{o} twist boundary with a fair coincidence site lattice (CSL), although Mg-doped $Co_{3-\delta}O_4$ spinel also occurred in the Co-rich specimen.[1] Such MgO-$Co_{1-x}O$ alloyed nanocondensates, with paracrystals hardly arranged as array along a specific crystallographic habit plane of the rocksalt- or spinel-type host, were found to catalyze the carbonaceous support to form turbostratic graphene shell upon radiant heating in the PLA process.[1] On the other hand, PLA of MgO powder in water resulted in the formation of rocksalt-type periclase nanoparticles which tended to have {111} habit planes parallel to the basal layers of lamellar brucite-like flakes more or less rolled as fibers, ribbons and tubes.[12] Such periclase nanoparticles were also found to nucleate at the edge of the lamellae and/or brucite flakes despite their chiral rolling. [12]

Here, rocksalt-type based particles were further synthesized by PLA of MgO-$Co_{1-x}O$ alloyed powders in water. We focused on: (1) phase selection of rocksalt-type based oxides and LDH, if any, (2) (hkl)-specific defects of the rocksalt-type based oxides, i.e. free surface, special grain boundary and the unique array of paracrystalline distribution of defect clusters, (3) Mg-Co interdiffusion and/or H^+ dopant dependence of the defects. Such knowledge sheds light on defect cluster and dynamic phase behavior of the $Co_{1-x}O$-MgO-H_2O system in natural occurrence such as the interior of the Earth where cobalt may possibly replace iron in the predominant magnesiowüstite in view of the Fe-Co-Ni content in some planetary materials (cf. Ref. [13] and references cited therein). In addition, the metastable composite nanocondensates/particulates with special shape, interface and defect clusters would widen the optocatalytic applications of the undoped cobalt oxides in thin film or bulk.[14-17]

2. Experimental

The $(Mg_{0.9}Co_{0.1})O$, $(Mg_{0.5}Co_{0.5})O$ and $(Mg_{0.1}Co_{0.9})O$ solid solution powders (SSP), hereafter refer to M9C1, M5C5 and M1C9 for the specified molar ratios, were prepared by dry pressing the mixed end member powders, i.e. MgO (CERAC, 99.5%) and $Co(OH)_2$ (SINOXP 99.5%) into disks (16 mm in diameter) for firing at 1100°C for 3 h and then furnace cooling followed by grinding with agate mortar and pestle to become powders less than ca. 45 μm (i.e. 325 mesh) in size (Supplement Fig. 1). The M9C1, M5C5 and M1C9 SSPs with predominant rocksalt-type phase and additional minor Mg-doped $Co_{3-\delta}O_4$ spinel phase for M1C9 (Supplement Fig. 2), along with $Co_{1-x}O$ powder of rocksalt-type structure (Aldrich, 99.99%, 325 mesh) were subjected to pulsed laser ablation (PLA) in water for 5 min using Nd-YAG-laser (Lotis, 1064 nm, beam mode: TEM00). In such experiments, the above powders were put in a silica test tube (8 mm diameter) filled with de-ionized water at a specified height of 10 mm for a total concentration of 3.2 mg/cc. Laser beam was focused to a spot size of 0.03 mm^2 on a specified water/focus height of 10 mm, i.e. at water level, under laser pulse energy of 300 mJ/pulse using second harmonic excitation, i.e. 532 nm for better laser penetration in water. The Q-switch mode for specified pulse duration of 16 ns was adopted to achieve a peak power density of 6.25×10^{10} W/cm^2 (average power density 1.00×10^4 W/cm^2) at 10 Hz.

The UV-visible absorption of the colloidal suspension as-formed by PLA in water was characterized by the instrument of U-3900H, Hitachi, with a resolution of 0.1 nm in the range of 190 to 900 nm. The condensates were also collected on silica glass slide for phase identification by X-ray diffraction (XRD, SIEMENS D5000, Cu Kα at 40 kV, 30 mA and 3 s for each 0.05° increment from 10 up to 80 or 120 degrees of 2θ angle) and for their assembly observations by optical polarized microscopy. The crystal structures of the individual condensates collected on Cu grids overlaid with a carbon-coated collodion film were characterized by transmission electron microscopy (TEM, JEOL 3010 at 200 kV) based on bight field image (BFI) and selected area electron diffraction (SAED) and lattice image coupled with 2-D Fourier transform. The internal compressive stress of the nanocondensates was estimated from the refined electron diffraction lattice parameters using the Birch-Murnaghan equation of state[18,19] and the interpolated compressibility data of the end members MgO[20,21] and CoO.[22]

3. Results

3.1, XRD

The XRD traces of the samples as fabricated by PLA of M9C1, M5C5, M1C9 and $Co_{1-x}O$ powders in water for 5 min (Figs. 1a to 1d) showed clear diffractions of the predominant rocksalt-type phase, although minor spinel phase was also identified as Mg-doped $Co_{3-\delta}O_4$ in M1C9 specimen (Fig. 1c) and as $Co_{3-\delta}O_4$ in $Co_{1-x}O$ specimen (Fig. 1d).

3.2. TEM

3.2.1. M9C1

TEM BFI, DFI and SAED pattern (Figs. 2a to 2c) of the individual rocksalt-type $(Mg_xCo_{1-x})O$ particle produced by PLA of M9C1 in water showed well-developed {001} faces and {011} facets edge on in the [100] zone axis. Abundant dislocations and/or loops in the particle account for the Bragg diffraction contrast in DFI (Fig. 2b). EDX analysis (Fig. 2d) indicated the particle has composition close to the original M9C1 stoichiometry.

3.2.2. M5C5

By contrast, the (MgCo)O particle produced by PLA of M5C5 in water has rough surface yet (hkl)-specific array of paracrystalline distribution of defect clusters along with parallel epitaxial intergrowth of the spinel-type. This in manifested by TEM BFI (Fig. 3a), SAED pattern (Fig. 3b) and lattice image (Fig. 3c) of a typical particle with weak {202} spinel diffractions in the $[11\bar{1}]$ zone axis. The 2-D Fourier transform (Fig. 3d) coupled with enlarged lattice image (Fig. 3e) and inverse Fourier transform (Fig. 3f) of the rocksalt-type domain further showed the paracrystalline array of defect clusters (ca. 1.5 nm interspacing) following $(1\bar{2}\bar{1})$ plane edge on in the $[11\bar{1}]$ zone axis. It should be noted that the rocksalt-type nanocondensates and amorphous phase in the matrix account for the diffraction rings and diffuse diffraction, respectively in the SAED pattern (Fig. 3b).

The paracrystal array was also found to follow the {311} planes for the rocksalt-type domain in the same specimen. This is indicated by TEM lattice image (Fig. 4a), 2-D forward Fourier transform (Fig. 4b) coupled with enlarged lattice image (Fig. 4c) and inverse Fourier transform (Fig. 4d) of the square region showing two sets of paracrystal distribution of defect clusters following $(31\bar{1})$ and $(3\bar{1}1)$ planes edge on in the [011] zone axis with corresponding side band diffractions in the reciprocal space.

The observed wavelength $\lambda \sim 1.5$ nm for ~(111) vicinal (i.e. {112} and {113}-specific) paracrystal array can hardly be explained by $Mg(OH)_2$ LDH or 1-D lamellar phase which typically occur as a shell around the $(Mg_xCo_{1-x})O$ condensate by PLA of bulk alloy target in air under the influence of radiant heating during the PLA process.[1] (The predominant $(Co_xMg_{1-x})O$ protoxide nanocondensates were able to turn the carbonaceous support into turbostratic graphene shell upon radiant heating in such case.[1]) The ~(111) vicinal paracrystal array may be due to relatively high concentration of defect clusters for this M5C5 composition beside the influence of H^+ dopant as addressed later.

3.2.3. M1C9

TEM lattice image of a typical rocksalt-type (Mg_xCo_{1-x})O particle produced by PLA of M1C9 in water showed parallel-epitaxial spinel at the particle edge with characteristic ($\bar{1}11$) lattice fringes (Fig. 5a). The 2-D forward Fourier transform (Fig. 5b) coupled with enlarged lattice image (Fig. 5c) and inverse Fourier transform (Fig, 5d) of the inner area further showed paracrystalline distribution of defect clusters and the parallel-epitaxial spinel extension from the particle edge.

Occasionally, the spinel-type particles with well-developed face were coalesced in the same M1C9 specimen to form the [110] ($\bar{1}11$)/($\bar{1}12$) asymmetrical tilt boundary as shown edge on in the [$\bar{1}12$] zone axis by TEM lattice image (Fig. 6a), 2-D Fourier transform (Fig. 6b) coupled with enlarged (Fig. 6c) and inverse Fourier transform (Fig. 6d) of the square region.

3.2.4. $Co_{1-x}O$

As for the particles produced by PLA of $Co_{1-x}O$ in water, they are a mixture of rocksalt-type $Co_{1-x}O$ and spinel-type $Co_{3-\delta}O_4$ with bimodal size distribution according to TEM BFI (Fig. 7a) and SAED pattern (Fig. 7b).

TEM lattice image (Fig. 8a), 2-D Fourier transform (Fig. 8b) coupled with enlarged (Fig. 8c) and inverse Fourier transform (Fig. 8d) of the square region in this specimen further showed a typical rocksalt-type $Co_{1-x}O$ particle with well-developed ($1\bar{1}1$) face edge on in the [110] zone axis having weak $Co_{3-\delta}O_4$ spinel diffraction in comparison with the strong diffraction of the paracrystal array following ($\bar{1}1\bar{5}$) plane. The paracrystalline $Co_{1-x}O$/$Co_{3-\delta}O_4$ composite particle with irregular shape in association with a pore ca. 40 nm in diameter was also identified in the [141] zone axis (Fig. 9).

3.3. UV-visible absorbance and optical polarized microscopy

The UV-visible absorption spectra of the samples produced by PLA of M9C1, M5C5, M1C9 and $Co_{1-x}O$ in water (Figs. 10a, 10b, 10c and 10d) showed absorbance peaks with extrapolation to 234, 238, 237 and 235 nm corresponding to an apparent minimum band gap of 5.3, 5.2, 5.2 and 5.3 eV, respectively. (The absorption peak of these specimens would be due to charge transfer of Co-rich domains in the MgO and/or Co-O-H matrix rather than minimum band gap as addressed later.)

Optical polarized micrographs of the samples produced by PLA of M9C1, M5C5, M1C9 and $Co_{1-x}O$ in water and then assembled on a silica glass slide were taken without analyzer (Supplement Fig. 3a), under crossed polarizers (Supplement Fig. 3b), and crossed polarizers with additional λ plate (Supplement Fig. 3c) to show the optical properties of the particulates and nanocondensates which were assembled as much larger islands (up to ca. 50 microns) as fairly resolved. They turned out to be brownish and/or darkish with slight birefringence for M9C1, M5C5, M1C9 specimens, but darkish for $Co_{1-x}O$ specimen.

4. Discussion

4.1. Defect chemistry for paracrystal formation

Paracrystalline distribution of defect clusters was found to occur in the particles of $(Co_xMg_{1-x})O$ protoxide in M5C5, M1C9 and $Co_{1-x}O$ specimens but not M9C1 specimen when produced by PLA in water. Such defect clusters can be rationalized by the defect chemistry in the rocksalt-type structure with specific point defect species as in the following.

A larger lattice parameter for CoO (0.4261 nm, JCPDS file 75-1550) than MgO (0.4211 nm, JCPDS file 45-0946) indicated that Mg^{2+} (effective ionic radii, 0.0720 nm) was replaced by Co^{2+} in high spin (0.0745 nm) rather than low spin state (0.066 nm) in CN 6[23] of the rocksalt-type structure in M5C5 and M1C9 specimens. The oversized dopant Co^{2+} in the Mg^{2+} site could also force further Co ion to enter the interstitial site as $Co_i^{\bullet\bullet\bullet}$, which then induced charge-compensating cation vacancies and 4:1 defect clusters through the following equation in Kröger-Vink notation:[24]

$$2\text{CoO}\ \underline{\ \text{MgO}\ }\ \text{Co}_{\text{Mg}}^{x} + [\text{Co}_{i}^{\bullet\bullet\bullet} + 4\,\text{V}_{\text{Co}}'' + 5\text{h}^{\bullet}] + 2\text{O}_{\text{O}}^{x} \qquad (1)$$

Here $\text{Co}_{\text{Mg}}^{x}$ signifies a noncharged cobalt at magnesium sites in the crystal lattice and h could be associated with V_{Co}'' to form V_{Co}' or associated with $\text{Co}_{\text{Mg}}^{x}$ to form $\text{Co}_{\text{Mg}}^{\bullet}$. The resultant 4:1 type defect clusters can then be assembled to form paracrystalline ordered state in $(\text{Co}_x\text{Mg}_{1-x})\text{O}$ protoxide and then occasional Mg-doped $\text{Co}_{3-\delta}\text{O}_4$ spinel with a specified interspacing (1.5 to 2 nm on the average) of defect clusters in the individual particles. Alternatively, MgO may be directly doped with Co^{3+} by the following equation:

$$\text{Co}_2\text{O}_3\ \underline{\ \text{MgO}\ }\ \text{Co}_{\text{Mg}}^{\bullet} + [\text{Co}_{i}^{\bullet\bullet\bullet} + 4\,\text{V}_{\text{Co}}'' + 4\text{h}^{\bullet}] + 3\text{O}_{\text{O}}^{x} \qquad (2)$$

As for the paracrystal hosted by Co_{1-x}O, its formation would involve Co^{3+} residence in the interstitial tetrahedral site below 900°C to form 4:1 clusters and hence paracrystal in the spinel-type structure of $\text{Co}_{3-\delta}\text{O}_4$ even without Mg^{2+} dopant.[7]

The reason for the paracrystal to form arrays following the ~{111} vicinal planes of the rocksalt-type host, i.e. {112} and {113} for M5C5 and {115} for Co_{1-x}O would have something to do with the preferential distribution of Mg/Co cation and/or H^+ dopant- induced vacancies along the ~{111} vicinal planes presumably with {111} terraces and ledges for efficient transport of the point defect species and interface movement. Such a ~{111} vicinal rather than the close packed (111) habit plane for defect clustering in rocksalt-type (Mg,Co)O and Co_{1-x}O may also have beneficial lower strain and interfacial energy under the influence of dopants. This is analogous to the case of extended planar defects in other transition metal oxides, such as (hkl)-specific crystallographic shear of TiO_{2-x} rutile under the influence of oxygen partial pressure[25] or Zn^{2+} dopant.[26]

4.2. Internal compressive stress of MgO-CoO alloy particles

To further understand what laser pulses have done with the M9C1, M5C5 and M1C9 solid solution powders and Co_{1-x}O powder, such as the possible internal stress built up by laser irradiation, the XRD peaks of the predominant rocksalt-type phase in the samples before (Supplement Fig. 2) and after the PLA process in water (Fig. 1) were used to refine the lattice parameters. The refined XRD lattice parameter of the predominant (Co_xMg_{1-x})O protoxide in M9C1, M5C5, M1C9 turned out to be 0.4219 nm, 0.4242 nm and 0.4259 nm respectively before PLA, whereas 0.4214 nm, 0.4232 nm and 0.4247 nm, respectively (Table 1) after PLA under a power density of 6.25x10^{10} W/cm^2 for 5 min in water. The $Co_{1-x}O$ nanocondensates produced by PLA in water also have a smaller refined cell parameter (0.4251 nm, cf. Table 1) than the starting CoO powder (0.4261 nm, JCPDS file 48-1719).

The lattice parameter changes in the target powders post test can be attributed to internal stress rather than negligible change of stoichiometry. The internal compressive stress of the (Mg_xCo_{1-x})O protoxide by such a PLA process was then estimated from the refined X-ray lattice parameters to be ca. 0.58, 1.22, 1.53 and 1.31 GPa, respectively using the Birch-Murnaghan equation of state[18,19] and the interpolated compressibility data of the end members MgO (B_o=160 GPa and B_o'=4.15)[20] and CoO (B_o=180 GPa and B_o'=3.82).[22]

Such internal compressive stress level (ca. 1 GPa) for the particles by PLA of alloy powders in water under 6.25x10^{10} W/cm^2 is about half that produced by PLA of alloy disk in air under a much lower peak power density (1.5x10^7 W/cm^2).[1] This indicates that the particles were significantly relaxed in water, especially for the Mg-rich specimen, despite the higher power density input and severe shock effect in water of the present PLA process.

4.3. Surface and special interface of the MgO-CoO alloy particles

The rocksalt-type (Co_xMg_{1-x})O particles produced by PLA of bulk alloy M9C1, M5C5 and M1C9 in air showed the surface preference {100}> {110}> {111}~ {021}~ {013}~ {311}.[1] By contrast, the present (Co_xMg_{1-x})O particles produced by PLA of powdery alloy M9C1, M5C5, M1C9 and $Co_{1-x}O$ in water have rather rough surface except M9C1 which showed well-developed {100} faces with {110} edges. This indicates that Mg/Co ratio and hydrogenation both affect significantly the crystal shape of the rocksalt-type oxide. In this connection, the undoped MgO also has the preference {100}> {110}> {111} in unhydroxylated state whereas {111}, {310} and {110} are more stable than {100} under hydroxylated condition.[27]

As for the Mg-doped $Co_{3-\delta}O_4$ nanocondensate in M1C9 produced by PLA in water, it has well-developed ~{111} vicinal planes for (hkl)-specific coalescence as the [110] asymmetrical $(\bar{1}11)/(\bar{1}12)$ tilt boundary (Fig. 6). This special grain boundary of the spinel-type structure has a rectangular CSL defined by the superimposed oxygen atoms along $[110]_A//[110]_B$ and $[\bar{1}1\bar{2}]_A//[\bar{1}1\bar{1}]_B$ (Fig. 11) analogous to the same tilt boundary of superimposed NiO film of rocksalt type structure (cf. Fig. 10e of ref.[28]).

The interatomic Coulombic interactions is also of concern to the formation of cation-anion mixed ~{111} vicinal surfaces (in comparison with the cation-anion unmixed {111} planes) for MeO-MgO alloy in rocksalt-type structure where Me is specific divalent transition metal ion. The size-mismatched Mg and Co ions and protons are expected to affect the interatomic Coulombic interactions of the cation-anion mixed surface as the driving force for oriented attachment to form special grain boundaries, such as the present [110] asymmetrical $(\bar{1}11)/(\bar{1}12)$ tilt boundary. It is an open question if solute trapping/segregation occurred at such ~{111} vicinal surfaces and tilt boundary to have space charge.

4.4. Implications

The undoped $Co_{1-x}O$ tends to be hydroxylated under ambient condition with humid air as $Co(OH)_2$ with plate-like shape.[5] There is also overwhelming equilibrium periclase/brucite ($MgO/Mg(OH)_2$) phase boundary for the MgO-H_2O system from 600°C up to 1000°C and ambient pressure up to 4 GPa[29] in accordance with the occurrence of brucite flakes more or less rolled as fibers, ribbons or tubes having basal plane parallel to {111} of periclase MgO nanocondensates produced by the similar PLA in water.[12] By contrast, the preferred formation of rocksalt-type MgO-CoO alloy with dislocations and/or paracrystalline distribution of defect clusters and amorphous phase (e.g. Fig. 3b) rather than LDH by the present PLA process in water implies that the phase stability field of LDH is rather restricted in MgO-CoO-H_2O ternary system under high pressure and temperature condition including natural dynamic settings such as a subducted oceanic plate[30] or a lightening/meteorite impact site of the Earth rich in water, Mg and transition metals. The formation of stable $[110](\bar{1}11)/(\bar{1}12)$ asymmetrical tilt boundary with fair CSL by ~{111}-specific coalescence of the Mg-doped $Co_{3-\delta}O_4$ particles also sheds light on the dynamic orientation mechanism of the spinel-type transition metal silicate, in particular the $(Fe,Mg)_2SiO_4$ spinel in the transition zone of the Earth's interior where thermal and shear-promoted phase transitions prevail.[31]

The rocksalt-type $Mg_xCo_{1-x}O$ oxides with paracrystalline array of defect clusters and spinel-type intergrowth by the present dynamic PLA process in water showed UV absorbance near 5 eV (5.3-5.2 eV) which is significantly different from that (3.2-3.5 eV) produced by PLA in air.[1] This indicates that charge transfer of isolated CoO_6 octahedral structure rather than minimum band gap is of concern to the UV absorption of such alloyed materials. The particles produced by PLA of $Co_{1-x}O$ in water also have UV absorbance near 5 eV, which agrees with the band gap energy of CoO single crystal (5.43 eV) based on spectroscopic ellipsometry measurement[32] but much higher than most experimental values (2.5-2.8 eV). This may be rationalized by a direct band gap of ~5 eV and an indirect band gap of 2.8 eV as suggested by later theoretical calculation using the hybrid density functional local density approximation.[33] In any case, the hydrogenated $Mg_xCo_{1-x}O$ and $Co_{1-x}O$ particles by the present PLA process in water have composition and stress dependent paracrystalline distribution of defect clusters, nonpolar {100}/{110} faces with ledges, and special grain boundaries to absorb UV light for potential optocatalytic applications such as high-temperature solar selective absorbers[15] and electrochromic devices.[16]

5. Conclusions

1. PLA of powdery CoO-MgO alloy (M9C1, M5C5, M1C9 and Co$_{1-x}$O) in water caused the formation of predominant rocksalt-type (Co$_x$Mg$_{1-x}$)O with internal compressive stress (up to ca. 1 GPa) and amorphous phase rather than LDH.
2. The submicron-sized Co$_x$Mg$_{1-x}$)O particles have well-developed {100} surface and abundant dislocations for M9C1 whereas rough surface and paracrystalline distribution of defect clusters (ca. 1.5-2 nm interspacing) along with spinel-type intergrowth for Co-richer compositions.
3. The paracrystal array follows the ~{111} vicinal planes of the rocksalt-type host, i.e. {112} and {113} for M5C5 and {115} for Co$_{1-x}$O due to mutual dopant and/or hydrogenation effect.
4. The stable $[110](\bar{1}11)/(\bar{1}12)$ asymmetrical tilt boundary with fair coincidence site lattice can be rationalized by {111}-specific coalescence of the spinel particles in M1C9 specimen.
5. The overall substances by the present dynamic PLA process in water showed UV absorbance near 5 eV.

Acknowledgments: This research was supported by Center for Nanoscience and Nanotechnology at NSYSU and partly by the Ministry of Science and Technology, Taiwan (ROC). We thank anonymous referees for constructive comments.

References

1 B.Y. Chen, S.S. Lin, P. Shen and S.Y. Chen, *CrystEngComm*, 2015, **17**, 4919.

2 J. Robin, *Ann. Chim.*, 1955, **10**, 397.

3 E.M. Levin, C.R. Robbins and H.F. McMurdie, *Phase diagram for ceramists*, (compiled at the Nation Bureau of Standard, edited and published by the American Ceramic Society Inc., 1964, Fig. 51)

4 S. Yagi, Y. Ichikawa, I. Yamada, T. Doi, T. Ichitsubo and E. Matsubara, *Jap. J. Appl. Phys.*, 2013, **52**, 02501.

5 Y. Yeh, I.H. Liu and P. Shen, *J. Eur. Ceram. Soc.*, 2010, **30**, 677.

6 M. Oku and Y. Sato, *Appl. Surf. Sci.*, 1992, **55**, 37.

7 W.H. Lee and P. Shen, *J. Solid State Chem.*, 2004, **177**, 101.

8 M.Y. Li and P. Shen, *Mater. Sci. Eng. B*, 2004, **111**, 82.

9 T.M. Tsai, K.C. Yang and P. Shen, *J. Solid State Chem.*, 2004, **177**, 3301.

10 C.N.Huang, P. Shen and K.Y. Hsieh, *J. Eur. Ceram. Soc.*, 2007, **27**, 4685.

11 C.N. Huang, S.Y. Chen, M.H. Tsai and P. Shen, *J. Cryst. Growth*, 2007, **305**, 285.

12 P.J. Chen, C.H. Wu, P. Shen and S.Y. Chen, *Appl. Phys. A*, 2014, **116**, 823.

13 J.J. Papike, Planetary materials, in *Reviews in Mineralogy*, ed. P. H. Ribbe, Mineral. Soc. Am., 1998, vol. 36.

14 E.M. Logothesis, A.H. Meitzler and K.R. Laud, *Appl. Phys. Lett.*, 1975, **26**, 209.

15 G.B. Smith, A. Ignatiev and G. Zajac, *J. Appl. Phys.*, 1980, **51**, 4186.

16 T. Maruyama and S. Arai, *J. Electrochem. Soc.*, 1996, **143**, 1383.

17 M. Ando, T. Kobayashi, S. Kobayashi, and M. Haruta, *J. Mater. Chem.*, 1997, **7**, 1779.

18 J.P. Poirier and A. Tarantola, *Phys. Earth Planet. Inter.*, 1998, 109, 1.

19 J.P. Poirier, *Introduction to the physics of the Earth's interior*, Edition 2, (Cambridge University Press, Cambridge, 2000)

20 Y.W. Fei, *Am. Mineral..* 1999, **84**, 272.

21 S. Rekhi, S.K. Saxena, Z.D. Atlasa and J. Hub, *Solid State Commun*., 2001, **117**, 33.

22 Q. Guo, H.K. Mao, J.Z. Hu, J.F. Shu and R.J. Hemley, *J. Phys.: Condens. Matter*, 2002, **14**, 11369.

23 R.D. Shannon, *Acta Crystallogr A*, 1976, **32**, 751.

24 F.A. Kröger and H.J. Vink, *Solid State Phys*., 1956, **3**, 307.

25 C.R.A. Catlow, Defect clustering in nonstoichiometric oxides, in Sørensen O.T., *Nonstoichiometric oxides*, Academic Press Inc., New York, New York pp. 61-98.

26 T. Chen and P. Shen, *J. Phys. Chem. C*, 2009, **113**, 328.

27 N.H. de Leeuw, G.W. Watson and S.C. Parker, *J. Phys. Chem*., 1995, **99**, 17219.

28 S.W. Yeh, Y.J. Ji, H.L. Huang, D. Gan and P. Shen, *Journal of Physical Chemistry C*, 2010, **114**, 18886.

29 L.G. Liu and W.A. Bassett, *Elements, oxides, and silicates: high pressure phases with implications for the earth's interior*, Oxford University Press, New York, 1986.

30 R.J. Stern, *Reviews of Geophysics*, 2002, **40**, 1012.

31. T.C. Wu, W.A. Bassett, P.C. Burnley, M.S. Weathers, *J. Geophys. Res. B*, 1993, **98**, 19767.

32 T.D. Kang, H.S. Lee and H. Lee, *J. Korean Phys. Society*, 2007, **50**, 632.

33 R. Gillen and J. Robertson, *J. Phys.: Condens. Matter*, 2013, **25**, 165502-1-9.

Table 1. Refined XRD cell parameter (±0.0001 nm) of rocksalt-type particles in M9C1, M5C5, M1C9 and $Co_{1-x}O$ specimens produced by PLA in water for 5 min.

(hkl)	M9C1	M5C5	M1C9	$Co_{1-x}O$
	Obs./Refined	Obs./Refined	Obs./Refined	Obs./Refined
111	0.2434/0.2433	0.2444/0.2444	0.2450/0.2452	0.2453/0.2455
200	0.2106/0.2107	0.2116/0.2116	0.2128/0.2124	0.2125/0.2126
220	0.1490/0.1490	0.1496/0.1496	0.1498/0.1502	0.1502/0.1503
311	0.1268/0.1270	0.1276/0.1276	0.1280/0.1281	0.1284/0.1282
222	0.1217/0.1216	0.1233/0.1222	0.1228/0.1226	0.1229/0.1227
	a = 0.4214	***a*** = 0.4232	***a*** = 0.4247	***a*** = 0.4251

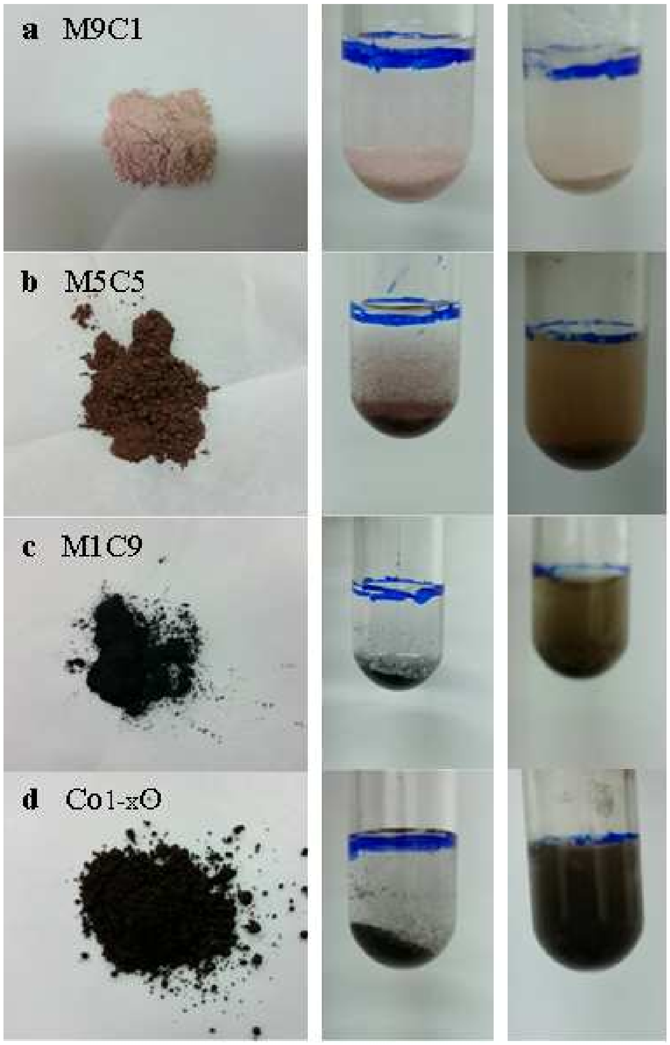

Supplement Figure 1. Photos of (a) M9C1, (b) M5C5 and (c) M1C9 solid solution powders (SSP) by reactive sintering at 1100°C for 3 h in air followed by grinding to be smaller than 100 µm in size (left panel) and then dispersion in water (middle panel) for PLA in water for 5 min (right panel). For comparison, the $Co_{1-x}O$ powder of rocksalt-type structure (Aldrich, 325 mesh) was also subjected to PLA in water for 5 min as compiled in (d).

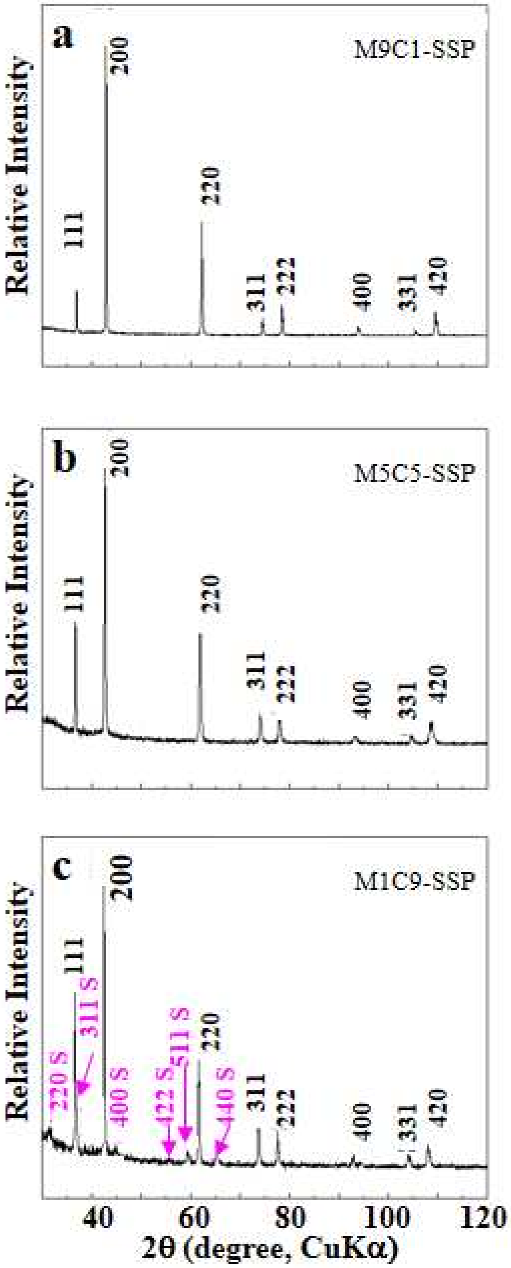

Supplement Figure 2. XRD traces of (a) M9C1, (b) M5C5 and (c) M1C9 solid solution powder with predominant rocksalt-type structure produced by a reactive sintering route (1100^{o}C for 3 h in open air) followed by grinding with a mortar and pestle. Note weak peaks of minor Mg-doped $Co_{3-\delta}O_4$ spinel in (c).

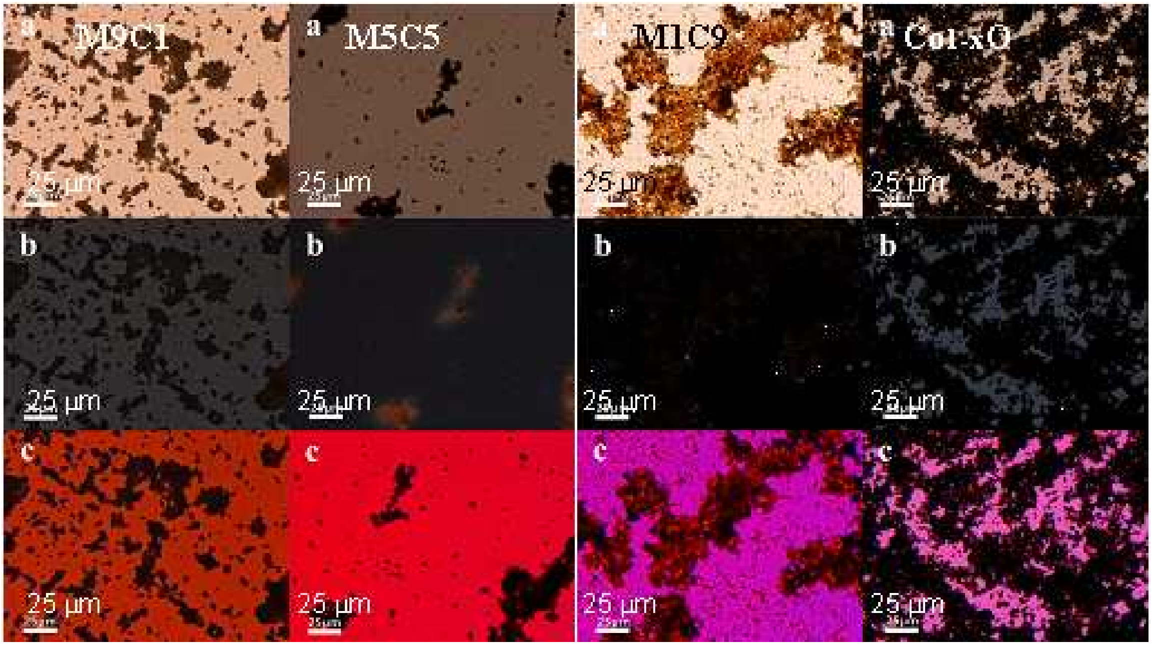

Supplement Figure 3. Optical polarized micrographs of the assembled particulates and nanocondensates, taken under (a) single polarizer, (b) crossed polarizers, (c) crossed polarizers with additional λ plate for the samples M9C1, M5C5, M1C9 and $Co_{1-x}O$ produced by PLA for 5 min in water showing brownish assembly and smaller sized individual particles with slight birefringence (cf. text). The scale bars, 25 µm.

Figure captions

Figure 1. XRD (CuKα) traces of rocksalt-type $(Mg_xCo_{1-x})O$ condensates produced by PLA of (a) M9C1, (b) M5C5, (c) M1C9 and (d) $Co_{1-x}O$ powder under Q-switch mode (6.25 x 10^{10} W/cm^2) and 10 mm water level (focus height) for 5 min. Note weak peaks of minor spinel of Mg-doped $Co_{3-\delta}O_4$ in (c) and $Co_{3-\delta}O_4$ in (d). The broad XRD peak around 20° 2θ is due to amorphous silica substrate.

Figure 2. TEM (a) BFI, (b) DFI (g=00$\bar{2}$), (c) SAED pattern and (d) EDX spectrum of rocksalt-type $(Mg_xCo_{1-x})O$ condensate with well-developed {001} faces and {011} facets edge on in the [100] zone axis) and defects (arrows in (b)) presumably dislocation loops. Sample produced by PLA of M9C1 in water.

Figure 3. TEM (a) BFI, (b) SAED pattern in the [11$\bar{1}$] zone axis of a typical particle with rocksalt-(r) and parallel-epitaxial spinel-type as manifested by the weak {202} diffractions circled, (c) lattice image taken from square region in (a), (d) 2-D Fourier transform coupled with (e) enlarged and (f) reconstructed image of the square region in (c) showing 1-D (1$\bar{2}\bar{1}$) paracrystalline (P) array of defect clusters in rocksalt-type domain. Note rocksalt-type nanocondensates and amorphous phase in the matrix account for the diffraction rings and diffuse diffraction, respectively in (b). Sample produced by PLA of M5C5 in water.

Figure 4. TEM (a) lattice image, (b) 2-D forward Fourier transform of the square region coupled with (c)/(d) enlarged lattice image and inverse Fourier transform, respectively showing paracrystalline (P) distribution of defect clusters (arrowed and circled) and double diffraction (D) of rocksalt-type (Mg,Co)O monoxide produced by PLA of M5C5 in water. Note the 2-D paracrystal array follows the {311}, i.e. (31$\bar{1}$) and (3$\bar{1}$1), host planes edge on in the [011] zone axis.

Figure 5. TEM (a) lattice image, (b) 2-D Fourier transform coupled with (c) enlarged and (d) reconstructed image of the square region in (a) showing paracrystalline (P as arrowed and circled) distribution of defect clusters in rocksalt-type $(Mg_xCo_{1-x})O$ condensate with

parallel-epitaxial spinel at particle edge as indicated by the $(\bar{1}11)$ lattice fringes in (c). Sample produced by PLA of M1C9 in water.

Figure 6. TEM (a) lattice image, (b) 2-D Fourier transform coupled with (c) enlarged and (d) reconstructed image of the square region in (a) showing a Mg-doped $Co_{3-\delta}O_4$ spinel nanoparticle B with well-developed (311) face edge on and $(\bar{1}12)$ face top view in the $[\bar{1}12]$ zone axis was coalesced over another $[\bar{1}11]$ oriented spinel nanoparticle A to form [110] $(\bar{1}11)/(\bar{1}12)$ tilt boundary (cf. text). Sample produced by PLA of M1C9 in water.

Figure 7. TEM (a) BFI and (b) SAED pattern of rocksalt-type $Co_{1-x}O$ and spinel-type $Co_{3-\delta}O_4$ condensate/particulates with bimodal size distribution and random orientation. Sample produced by PLA of $Co_{1-x}O$ powder in water.

Figure 8. TEM (a) lattice image, (b) 2-D Fourier transform coupled with (c) enlarged and (d) reconstructed image of the square region in (a) showing a rocksalt-type $Co_{1-x}O$ nanoparticle with weak $Co_{3-\delta}O_4$ spinel (S) diffraction, paracrystal (P, arrowed and circled) following $(\bar{1}1\bar{5})$ plane and well-developed $(1\bar{1}1)$ face edge on in the [110] zone axis. Sample produced by PLA of $Co_{1-x}O$ in water.

Figure 9. TEM (a) lattice image, (b) 2-D Fourier transform coupled with (c) enlarged and (d) reconstructed image of the square region in (a) showing a rocksalt-type $Co_{1-x}O$ nanoparticle with weak $Co_{3-\delta}O_4$ spinel (S) diffraction, paracrystal (P, arrowed and circled) in the [141] zone axis was associated with a pore produced by PLA of $Co_{1-x}O$ in water.

Figure 10. UV-visible absorption spectra of (a) M9C1, (b) M5C5, (c) M1C9 and (d) $Co_{1-x}O$ specimens produced by PLA in water.

Figure 11. Schematic drawing of the rectangular CSL of the $[110](\bar{1}11)/(\bar{1}12)$ asymmetrical tilt boundary of the coalesced spinel-type Mg-doped $Co_{3-\delta}O_4$ nanoparticles in Fig. 6.

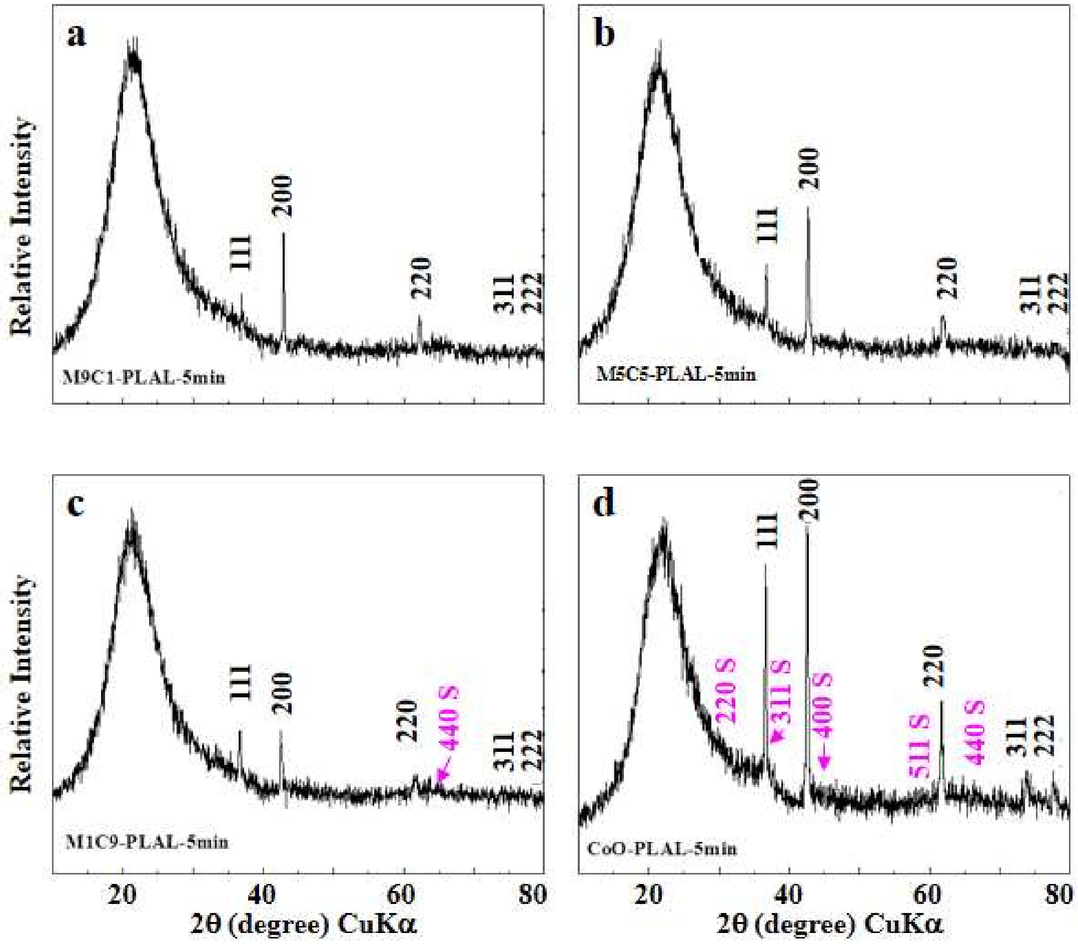

Figure 1. XRD (CuKα) traces of rocksalt-type $(Mg_xCo_{1-x})O$ condensates produced by PLA of (a) M9C1, (b) M5C5, (c) M1C9 and (d) $Co_{1-x}O$ powder under Q-switch mode (6.25×10^{10} W/cm^2) and 10 mm water level (focus height) for 5 min. Note weak peaks of minor spinel of Mg-doped $Co_{3-\delta}O_4$ in (c) and $Co_{3-\delta}O_4$ in (d). The broad XRD peak around 20^o 2θ is due to amorphous silica substrate.

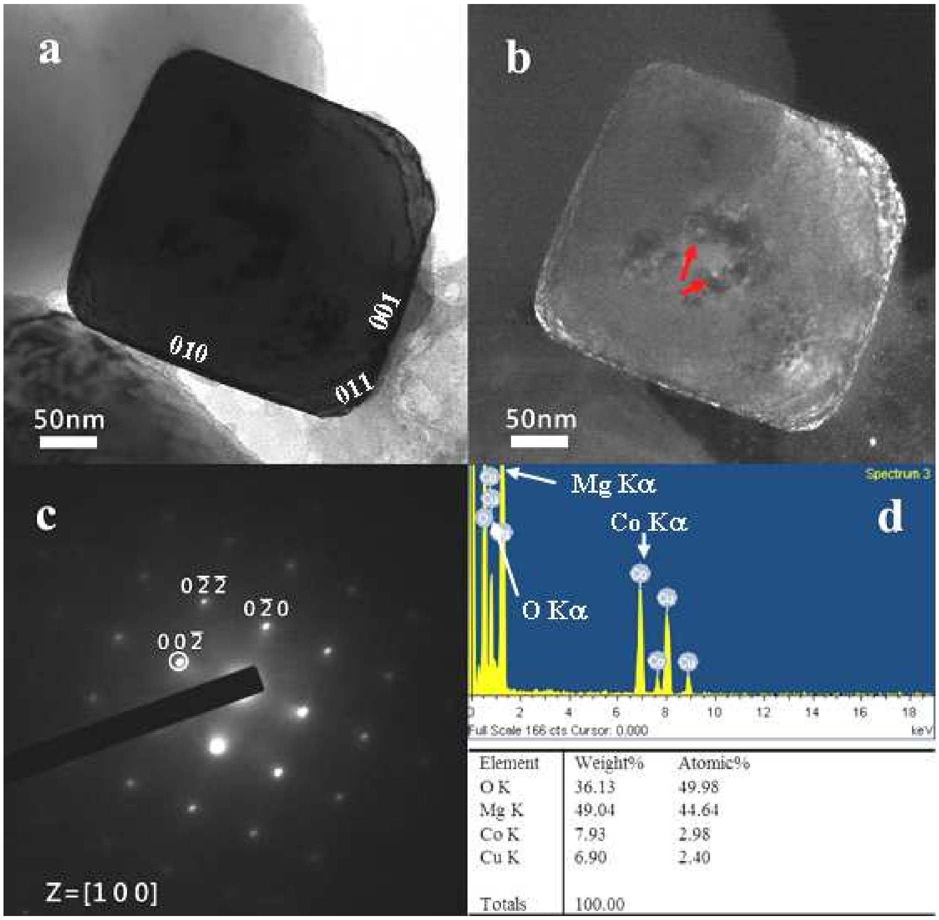

Element	Weight%	Atomic%
O K	36.13	49.98
Mg K	49.04	44.64
Co K	7.93	2.98
Cu K	6.90	2.40
Totals	100.00	

Figure 2. TEM (a) BFI, (b) DFI (g=00 $\bar{2}$), (c) SAED pattern and (d) EDX spectrum of rocksalt-type (Mg_xCo_{1-x})O condensate with well-developed {001} faces and {011} facets edge on in the [100] zone axis) and defects (arrows in (b)) presumably dislocation loops. Sample produced by PLA of M9C1 in water.

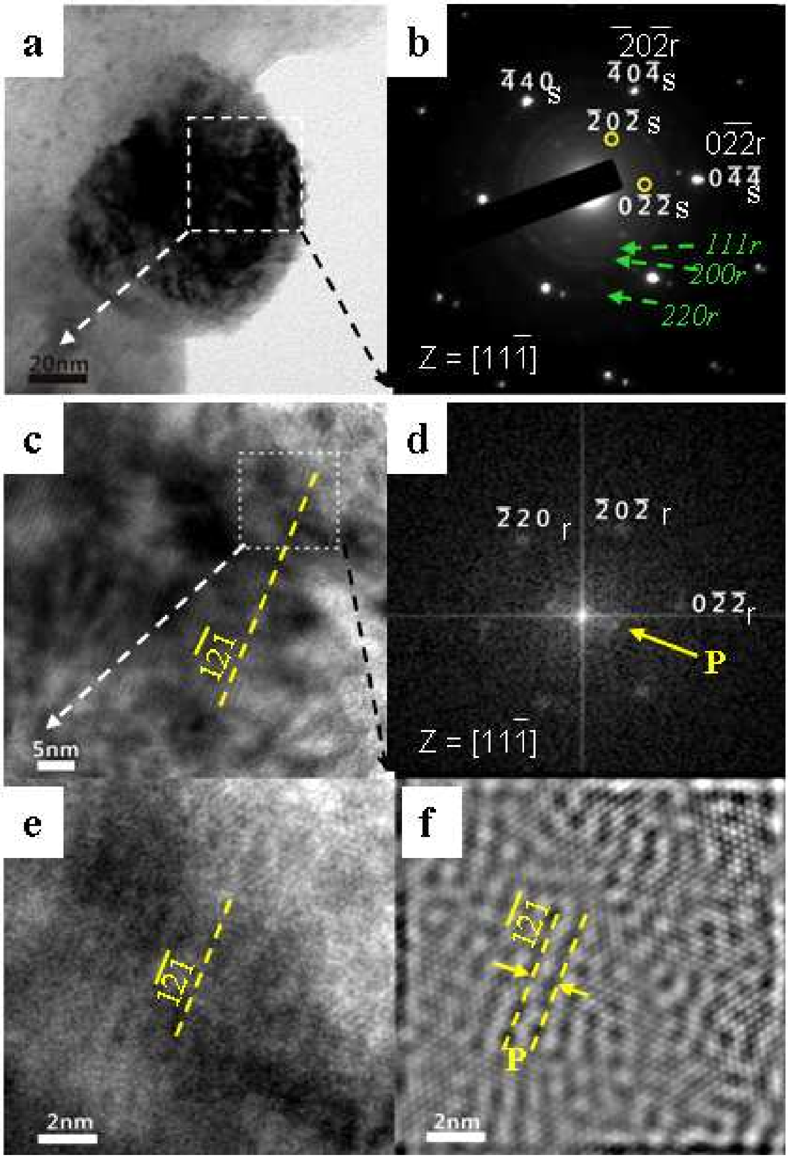

Figure 3. TEM (a) BFI, (b) SAED pattern in the [11$\bar{1}$] zone axis of a typical particle with rocksalt-(r) and parallel-epitaxial spinel-type as manifested by the weak {202} diffractions circled, (c) lattice image taken from square region in (a), (d) 2-D Fourier transform coupled with (e) enlarged and (f) reconstructed image of the square region in (c) showing 1-D (1$\bar{2}$$\bar{1}$) paracrystalline (P) array of defect clusters in rocksalt-type domain. Note rocksalt-type nanocondensates and amorphous phase in the matrix account for the diffraction rings and diffuse diffraction, respectively in (b). Sample produced by PLA of M5C5 in water.

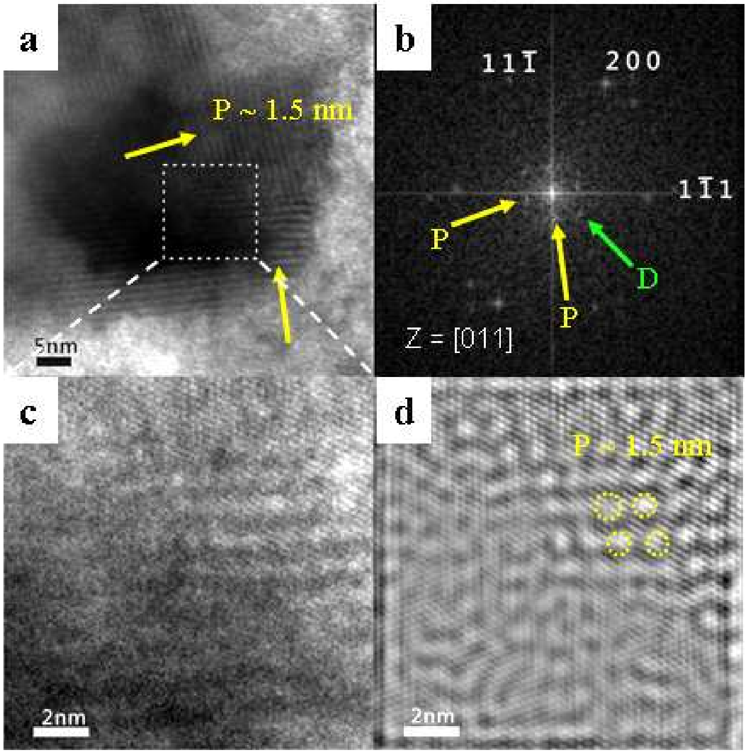

Figure 4. TEM (a) lattice image, (b) 2-D forward Fourier transform of the square region coupled with (c)/(d) enlarged lattice image and inverse Fourier transform, respectively showing paracrystalline (P) distribution of defect clusters (arrowed and circled) and double diffraction (D) of rocksalt-type (Mg,Co)O monoxide produced by PLA of M5C5 in water. Note the 2-D paracrystal array follows the {311}, i.e. $(31\bar{1})$ and $(3\bar{1}1)$, host planes edge on in the [011] zone axis.

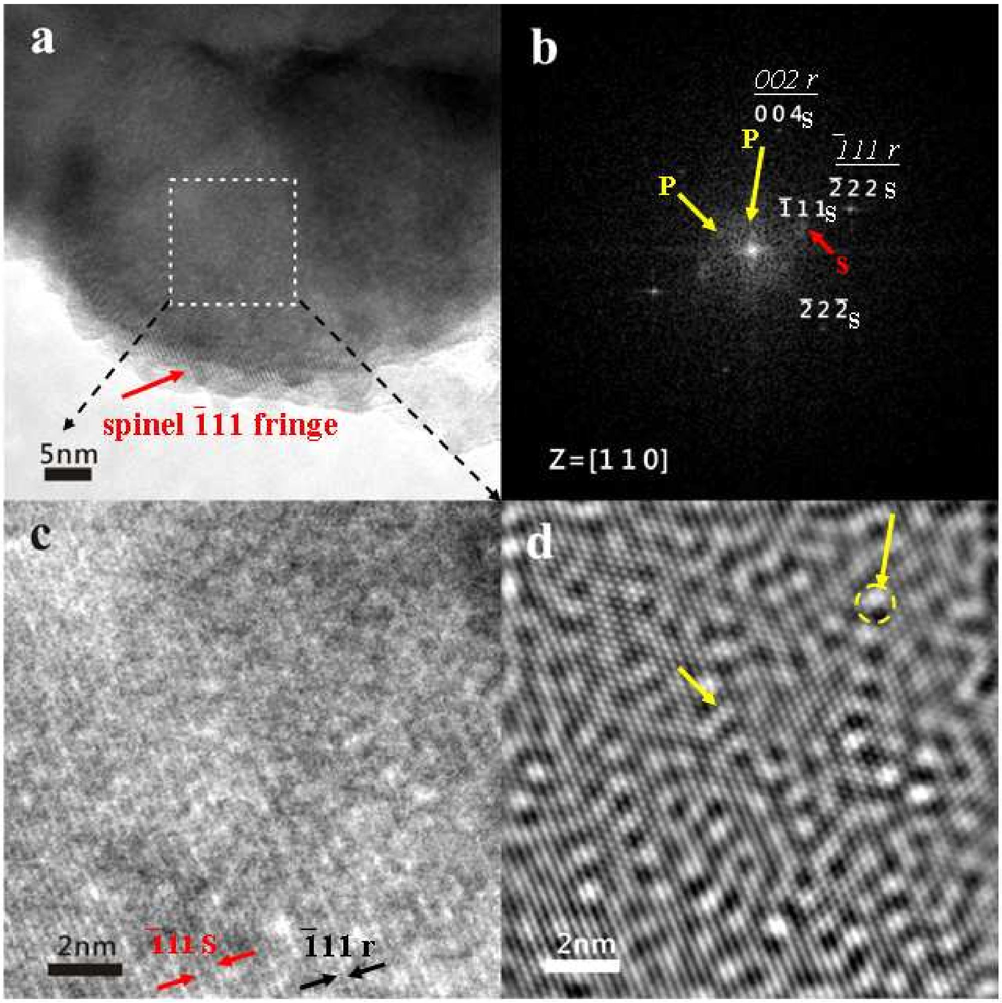

Figure 5. TEM (a) lattice image, (b) 2-D Fourier transform coupled with (c) enlarged and (d) reconstructed image of the square region in (a) showing paracrystalline (P as arrowed and circled) distribution of defect clusters in rocksalt-type ($(Mg_xCo_{1-x})O$) condensate with parallel-epitaxial spinel at particle edge as indicated by the ($\bar{1}$11) lattice fringes in (c). Sample produced by PLA of M1C9 in water.

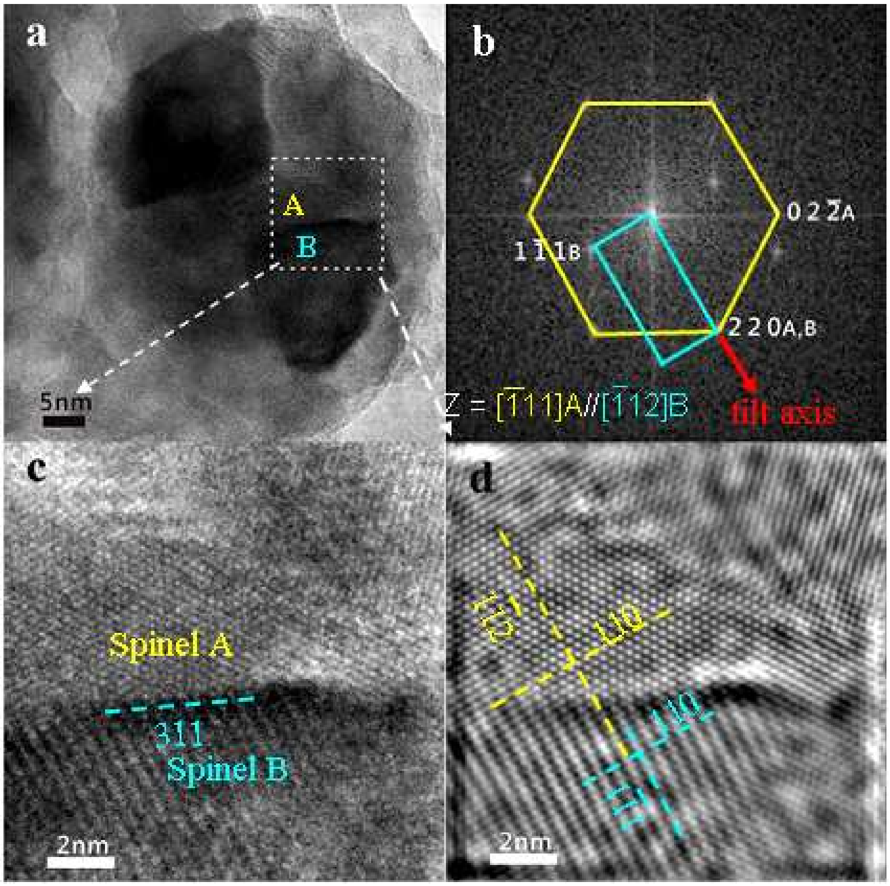

Figure 6. TEM (a) lattice image, (b) 2-D Fourier transform coupled with (c) enlarged and (d) reconstructed image of the square region in (a) showing a Mg-doped $Co_{3-\delta}O_4$ spinel nanoparticle B with well-developed (311) face edge on and $(\bar{1}12)$ face top view in the $[\bar{1}12]$ zone axis was coalesced over another $[\bar{1}11]$ oriented spinel nanoparticle A to form [110] $(\bar{1}11)/(\bar{1}12)$ tilt boundary (cf. text). Sample produced by PLA of M1C9 in water.

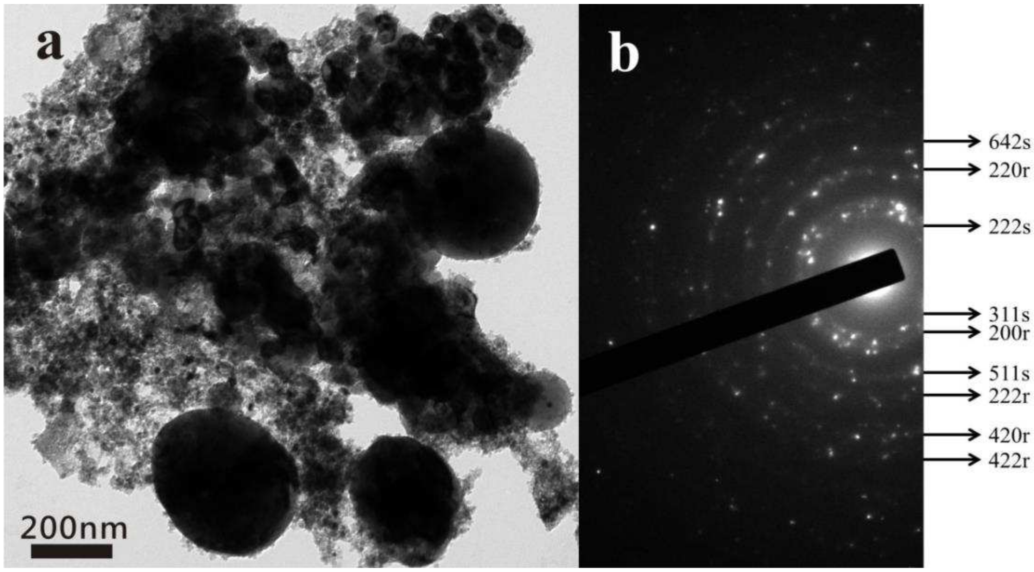

Figure 7. TEM (a) BFI and (b) SAED pattern of rocksalt-type $Co_{1-x}O$ and spinel-type $Co_{3-\delta}O_4$ condensate/particulates with bimodal size distribution and random orientation. Sample produced by PLA of $Co_{1-x}O$ powder in water.

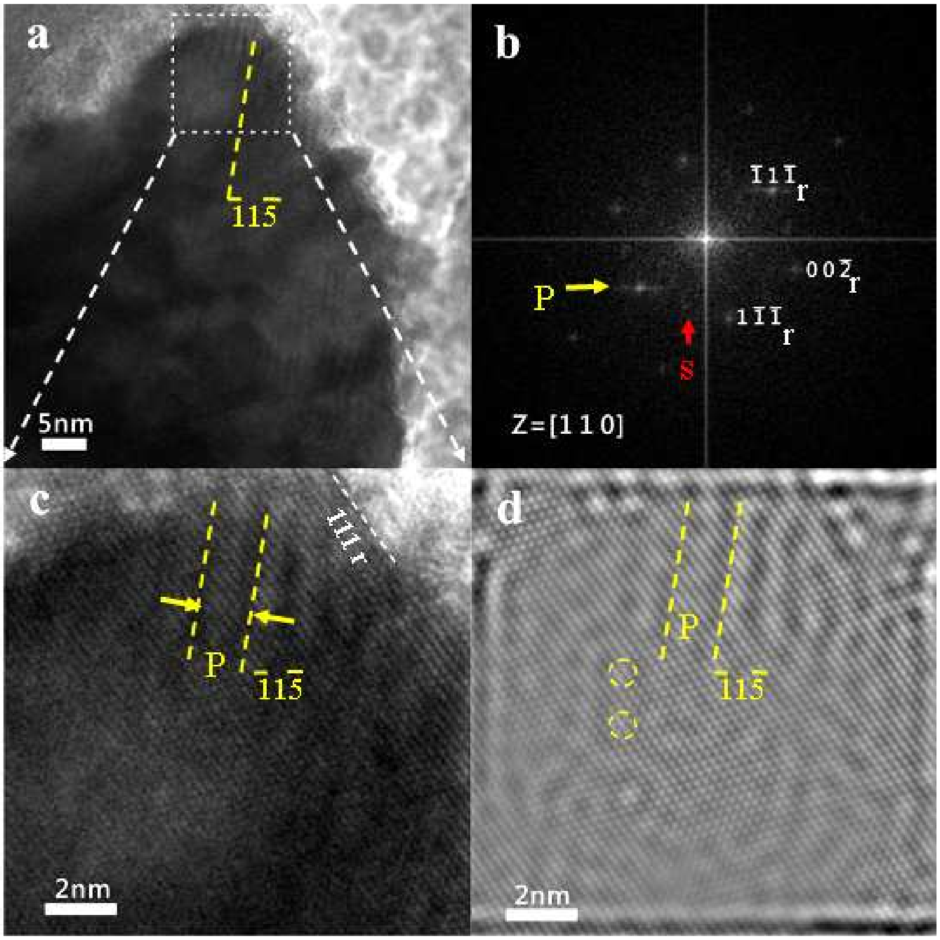

Figure 8. TEM (a) lattice image, (b) 2-D Fourier transform coupled with (c) enlarged and (d) reconstructed image of the square region in (a) showing a rocksalt-type Co$_{1-x}$O nanoparticle with weak Co$_{3-\delta}$O$_4$ spinel (S) diffraction, paracrystal (P, arrowed and circled) following ($\bar{1}1\bar{5}$) plane and well-developed ($1\bar{1}1$) face edge on in the [110] zone axis. Sample produced by PLA of Co$_{1-x}$O in water.

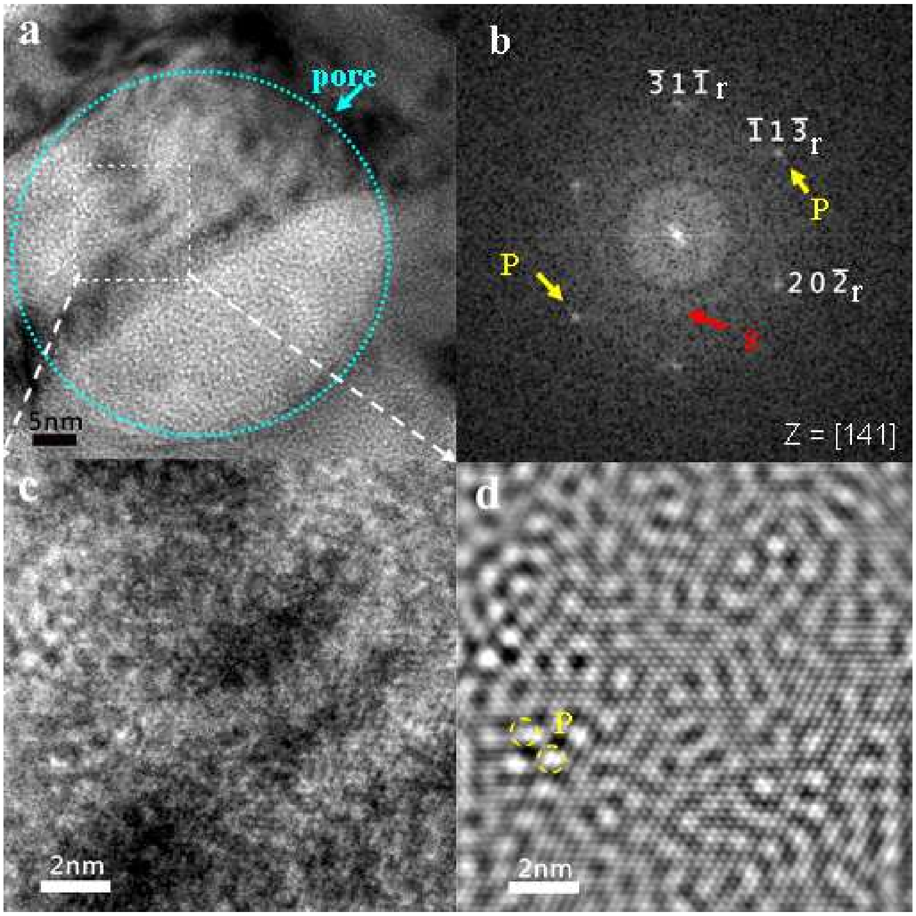

Figure 9. TEM (a) lattice image, (b) 2-D Fourier transform coupled with (c) enlarged and (d) reconstructed image of the square region in (a) showing a rocksalt-type $Co_{1-x}O$ nanoparticle with weak $Co_{3-\delta}O_4$ spinel (S) diffraction, paracrystal (P, arrowed and circled) in the [141] zone axis was associated with a pore produced by PLA of $Co_{1-x}O$ in water.

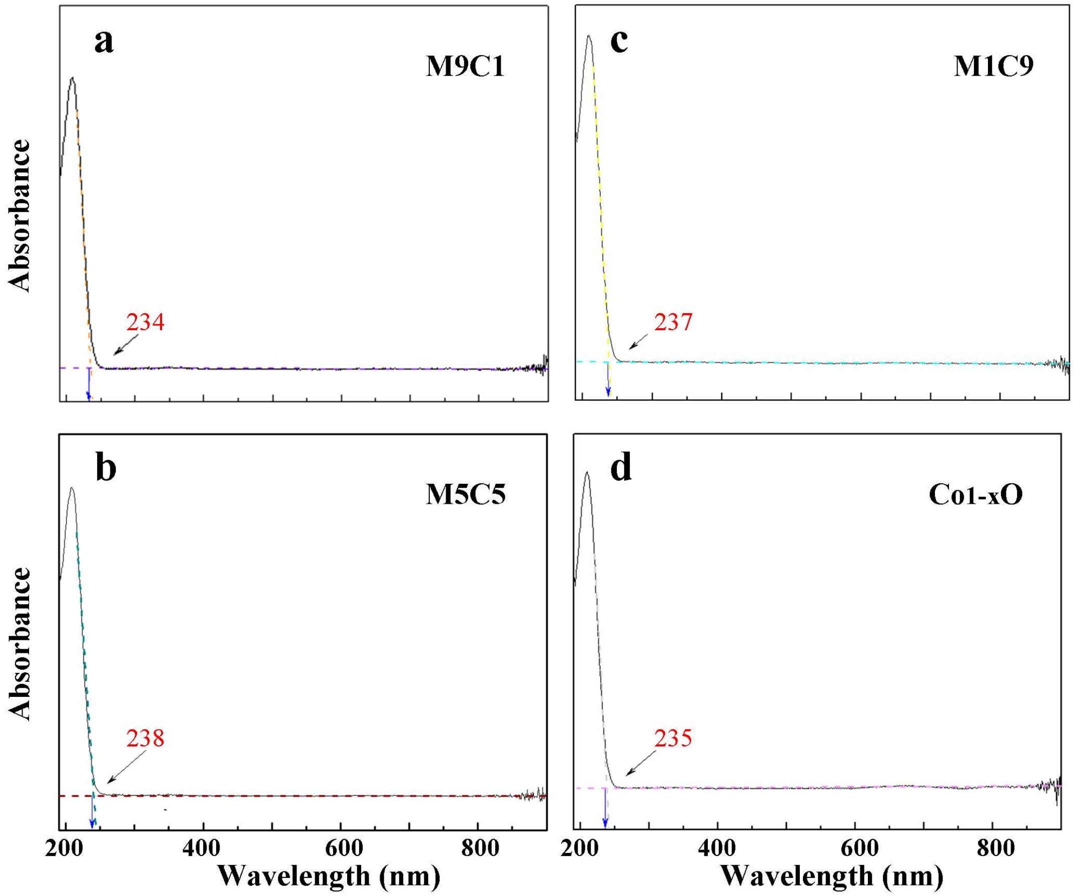

Figure 10. UV-visible absorption spectra of (a) M9C1, (b) M5C5, (c) M1C9 and (d) $Co_{1-x}O$ specimens produced by PLA in water.

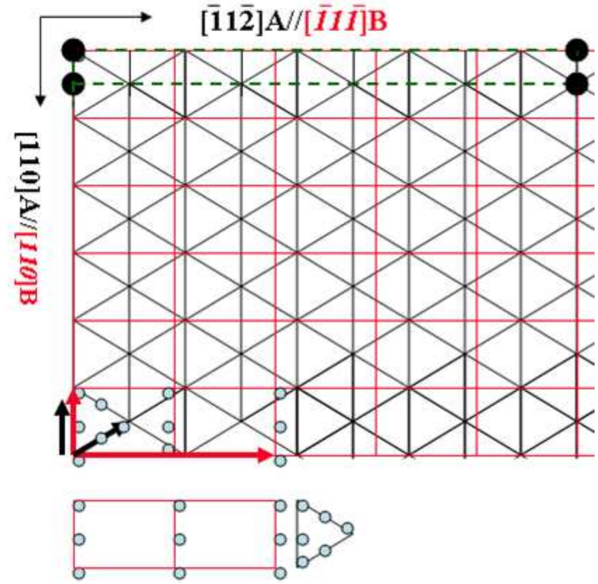

Figure 11. Schematic drawing of the rectangular CSL of the [110]($\bar{1}$11)/($\bar{1}$12) asymmetrical tilt boundary of the coalesced spinel-type Mg-doped $Co_{3-\delta}O_4$ nanoparticles in Fig. 6.

TOC

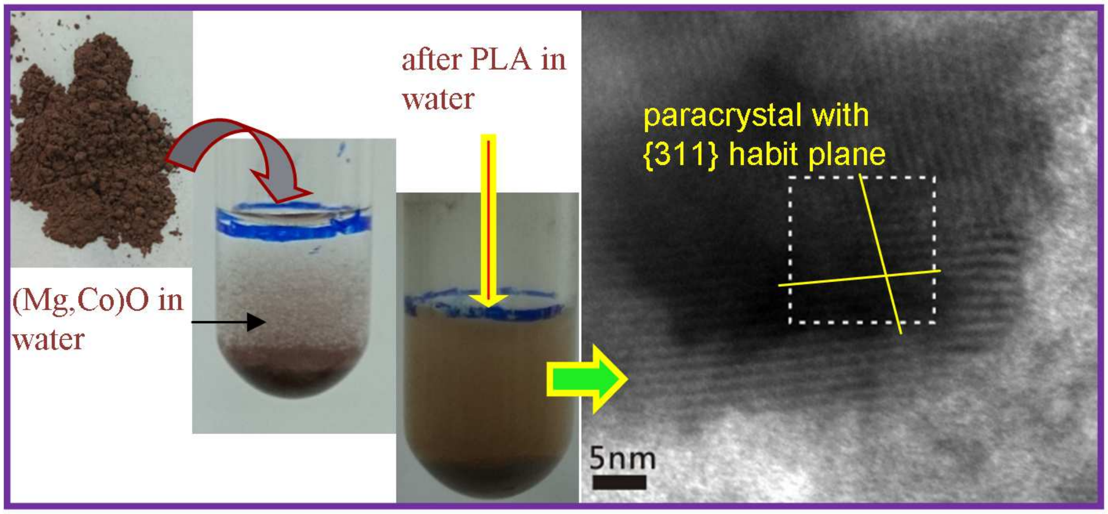

Legend: MgO-CoO particles with (hkl)-specific paracrystalline defects by pulsed laser ablation of solid-solution powders in water